Real-Time Feature Extraction From Electrocochleography With Impedance Measurements During Cochlear Implantation Using Linear State-Space Models

Raphael R. Andonie, Wilhelm Wimmer, Reto A. Wildhaber, Marco Caversaccio, and Stefan Weder

***Abstract*—Electrocochleography (ECochG) is increasingly used to monitor the inner ear function of cochlear implant (CI) patients during surgery. Current ECochG-based trauma detection shows low sensitivity and specificity and depends on visual analysis by experts. Trauma detection could be improved by including electric impedance data recorded simultaneously with the ECochG. However, combined recordings are rarely used because the impedance measurements produce artifacts in the ECochG. In this study, we propose a framework for automated real-time analysis of intraoperative ECochG signals using Autonomous Linear State-Space Models (ALSSMs). We developed ALSSM based algorithms for noise reduction, artifact removal, and feature extraction in ECochG. Feature extraction includes local amplitude and phase estimations and a confidence metric over the presence of a physiological response in a recording. We tested the algorithms in a controlled sensitivity analysis using simulations and validated them with real patient data recorded during surgeries. The results from simulation data show that the ALSSM method provides improved accuracy in the amplitude estimation together with a more robust confidence metric of ECochG signals compared to the state-of-the-art methods based on the fast Fourier transform (FFT). Tests with patient data showed promising clinical applicability and consistency with the findings from the simulations. We showed that ALSSMs are a valid tool for real-time analysis of ECochG recordings. Removal of artifacts using ALSSMs enables simultaneous recording of ECochG and impedance data. The proposed feature extraction method provides the means to automate the assessment of ECochG. Further validation of the algorithms in clinical data is needed.**

***Index Terms*—Autonomous linear state-space models, biomedical engineering, biomedical signal processing, biomedical telemetry, cochlear implants (CI), deafness, electrocochleography (ECochG), feature extraction, hearing preservation, impedance, real-time.**

Manuscript received 10 February 2023; revised 9 May 2023; accepted 12 May 2023. Date of publication 17 May 2023; date of current version 20 October 2023. This work was supported by Cochlear Ltd., Sydney, Australia. *(Corresponding author: Wilhelm Wimmer.)*

Raphael R. Andonie and Marco Caversaccio are with the Department of ENT, Head and Neck Surgery, Inselspital, Bern University Hospital, University of Bern, Switzerland, and also with the Hearing Research Laboratory, ARTORG Center for Biomedical Engineering Research, Bern University Hospital, University of Bern, Switzerland.

Wilhelm Wimmer is with the Department of ENT, Head and Neck Surgery, Inselspital, Bern University Hospital, University of Bern, 3010 Bern, Switzerland, with the Hearing Research Laboratory, ARTORG Center for Biomedical Engineering Research, Bern University Hospital, University of Bern, 3008 Bern, Switzerland, and also with the TUM School of Medicine, Klinikum rechts der Isar, Department of Otorhinolaryngology, Technical University of Munich, 80333 Munich, Germany (e-mail: wilhelm.wimmer@unibe.ch).

Reto A. Wildhaber is with the Institute for Medical Engineering and Medical Informatics, University of Applied Sciences and Arts Northwestern Switzerland, Switzerland, and also with the Signal and Information Processing Laboratory (ISI), ETH Zurich, Switzerland.

Stefan Weder is with the Department of ENT, Head and Neck Surgery, Inselspital, Bern University Hospital, University of Bern, Switzerland.

Digital Object Identifier 10.1109/TBME.2023.3276993

I. Introduction

COCHLEAR Implantation is a highly effective treatment for patients suffering from severe-to-profound hearing loss. For cochlear implant (CI) patients, an electrode array is placed in the inner ear to stimulate the auditory nerve fibers to transmit sound from an external microphone to the brain. To optimize the surgical and audiological outcome, it is crucial to preserve cochlear structure and function during implantation [1], [2], [3], [4].

Electrocochleography (ECochG) is increasingly used to monitor cochlear health during cochlear implantation [5], [6], [7], [8], [9], [10], [11], [12], [13], [14]. ECochG measures cochlear biopotentials in response to an acoustic stimulus. Using pure tone stimulation (i.e., sinusoidal stimulus), responses are commonly recorded in pairs, consisting of a rarefaction (RAR) and condensation (CON) response. RAR and CON refer to the polarity of the longitudinal pressure wave of the applied stimulus. Different response components can be derived from these ECochG signals, which are suggested to originate from different neurosensory sources within the cochlea [15]. The cochlear microphonic (CM) mainly indicates the function of the outer hair cells (OHC) and is an electrical reflection of the acoustic stimulus [16]. It is considered the ECochG component with the most predictive power regarding cochlear health [11], [17], [18], [19], [20]. To measure the CM, the difference signal (DIF) between CON and RAR is analyzed. However, acoustic

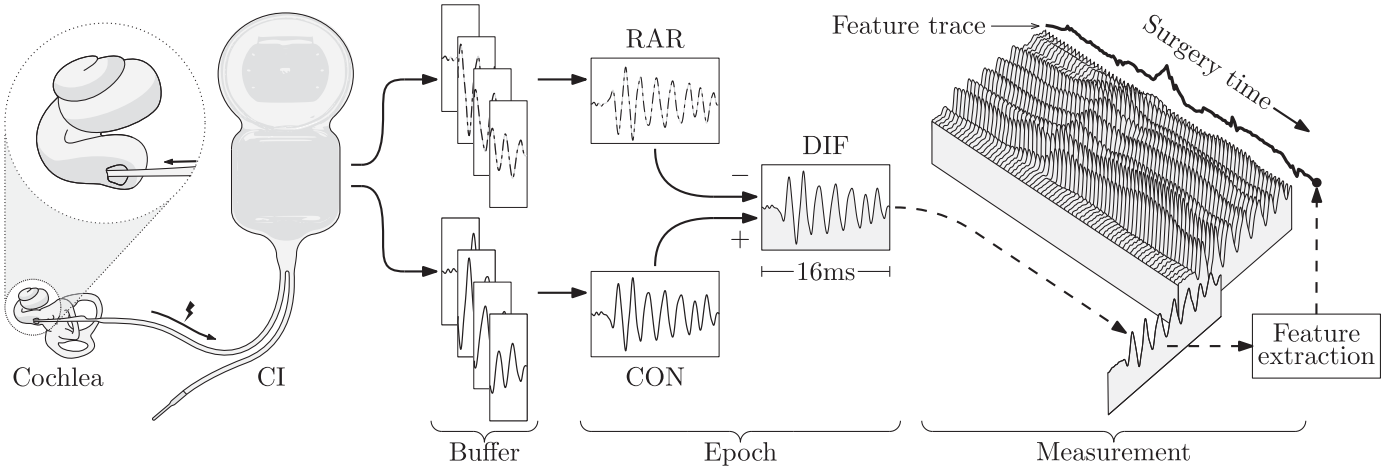

Fig. 1. Schematic overview of a typical intraoperative real-time Electrocochleography (rt-ECochG) measurement. The cochlea generates biopotentials as a response to acoustic stimulation. The rt-ECochG is recorded directly by the cochlear implant (CI) at the most apical intracochlear electrode, which is slowly inserted through the round window. The signal is digitized at a sampling rate $f_s = 20.5$ kHz and raw data chunks of a few milliseconds length are buffered before stitched together to form a full response. The time span of a response is denoted an *epoch* and lasts from 11 to 16 milliseconds. A response contains a condensation (CON) and rarefaction (RAR) response pair which result in the difference signal (DIF) after subtraction. The DIF signal is used to analyze the cochlear microphonic (CM), a commonly used component of the ECochG signal. The continuous recording of responses generates a sequence of epochs, which are combined into the rt-ECochG *measurement*. By extracting features from the individual responses, *feature traces* are created over the duration of a measurement, as shown here on the basis of the CM amplitude. We refer to a collection of feature traces as the *insertogram*.

harmonics in the measurements prevents perfect separation of the single response component [11], [21], [22].

We refer to real-time ECochG (rt-ECochG) as an ECochG that was continuously recorded and instantly processed during surgery [10]. A typical intracochlear rt-ECochG measurement recorded by the CI's most apical electrode during surgery is shown in Fig. 1. Individual *epochs* are composed of several buffers, which are acquired from repeatedly recorded responses. In this way, response pairs (CON and RAR) are recorded at a repetition rate of 1.25Hz. We obtain the DIF signal by subtracting the RAR from the CON responses. The continuous recording generates a sequence of epochs, referred to as the rt-ECochG *measurement*. By extracting features (e.g. CM amplitude or phase) from the epochs, *feature traces* are created over the duration of a measurement. We refer to the collection of different feature traces as the *insertogram*.

Studies have found a significant correlation between changes in CM amplitude during CI electrode insertion and postoperative preservation of residual hearing [4], [5], [23], [24]. However, existing methods for trauma detection show low sensitivity and specificity and are limited to functional preservation in patients with substantial residual hearing [13], [19]. Moreover, the current gold standard is the visual inspection of the ECochG signals by an expert, which prevents the integration of the analysis into an automated software [25], [26]. A promising strategy to achieve more reliable automatic trauma detection is to include more data such as the electrical impedance of the CI electrodes in the analysis in addition to the rt-ECochG amplitude features [27], [28], [29], [30], [31], [32]. Electrical impedance data provides information about the electrode-tissue interface, including the electrode-electrolyte interface and the surrounding tissue resistance [33]. The increased complexity due to the simultaneous measurement of rt-ECochG and impedance in real time (rt-impedance) as well as the extraction of more signal features poses new challenges to the signal processing methods applied. In this paper, we present a new method for real-time analysis of intraoperative rt-ECochG using autonomous linear state-space models (ALSSMs), enabling the simultaneous measurement of rt-impedance data. Our ALSSM based algorithms address a broad range of signal processing tasks such as artifact removal, filtering and feature extraction [34].

II. Materials and Methods

In this section, we briefly introduce the basics of ALSSM and how we use it to create algorithms for processing rt-ECochG. In addition, we show how we tested the performance of these new algorithms using simulation data and how we validated them in a visual proof of concept using exemplary real patient data. For comparison, we also applied an established standard method to both the simulations and the patient data.

A. ALSSMs as Signal Models

Model-based signal processing methods are well suited for the analysis of biological signals, as they allow to incorporate a priori knowledge of the signal physiology. ALSSMs enable the efficient online implementation of such model-based algorithms [34], [35], [36]. The ALSSMs in this study were implemented using the open source software library *lmlib* [37].

Discrete-time ALSSMs can generate functions such as polynomials, exponentials, and sinusoids, as well as linear combinations of those [38]. An ALSSM of order N is given by the

recursive state equation and the output equation

$$x_{i+1} = Ax_i \tag{1}$$

$$m_i = cx_i \tag{2}$$

with state transition matrix $A \in \mathbb{R}^{N\times N}$, output vector $c \in \mathbb{R}^{1\times N}$, state vector $x_i \in \mathbb{R}^N$, model output $m_i \in \mathbb{R}$, and time index $i \in \mathbb{Z}$.

Substitution of x_i in (2) with (1) leads to

$$m_i(x_0) = cA^i x_0 \tag{3}$$

with initial state vector x_0. Note that the output of a model, defined by A and c, is fully determined by the initial state x_0. For the sake of simplicity, we subsequently denote this initial state x_0 as x.

B. Localized ALSSM to Signal Fitting

The best approximation of an observed signal $y \in \mathbb{R}^K$ with K samples under the premise of a particular signal model is defined as the model output $m(\hat{x})$ yielding a minimal *cost* with respect to the squared error. For local signal approximation with ALSSMs in the interval $i \in \{a, \dots, b\}, a, b \in Z$, a *cost segment*

$$J_a^b(x, k; \gamma) = \sum_{i=k+a}^{k+b} \gamma^{i-k} \left(y_i - cA^{i-k}x\right)^2 \tag{4}$$

is used at filter index $k \in \mathbb{Z}$ [34]. γ^{i-k} adds a left- or right-sided exponentially decaying window to the cost term. By rewriting (4) in the form

$$J_a^b(x, k; \gamma) = x^\mathsf{T} W_k x - 2x^\mathsf{T}\xi_k + \kappa_k \tag{5}$$

with substitutes

$$W_k = \sum_{i=k+a}^{k+b} \gamma^{i-k} \left(A^{i-k}\right)^\mathsf{T} c^\mathsf{T} c A^{i-k} \in \mathbb{R}^{N\times N} \tag{6}$$

$$\xi_k = \sum_{i=k+a}^{k+b} \gamma^{i-k} y_i \left(A^{i-k}\right)^\mathsf{T} c^\mathsf{T} \in \mathbb{R}^N \tag{7}$$

$$\kappa_k = \sum_{i=k+a}^{k+b} \gamma^{i-k} y_i^2 \in \mathbb{R} \tag{8}$$

the actual computation can be performed in a sliding window manner and with minimum computational effort as a recursive least squares algorithm. In this case, the decaying window is essential to ensure numerical stability. Finally, the optimal state is given by

$$\hat{x}_k = \underset{x\in\mathbb{R}^N}{\operatorname{argmin}} J_a^b(x, k; \gamma) \tag{9}$$

$$= W_k^{-1}\xi_k. \tag{10}$$

as showed in [34].

C. Constrained Parameter Optimization

To achieve a desired behavior of the model, in many cases it is advantageous to restrict the space of solutions for (10) from $\mathbb{R}^N$ to a subspace of it. For a M dimensional subspace, we introduce the linear constraint

$$x = Hv \tag{11}$$

with the constraint matrix $H \in \mathbb{R}^{N\times M}$. The minimization problem (10) then modifies to

$$\hat{v}_k = \underset{v\in\mathbb{R}^M}{\operatorname{argmin}} J_a^b(Hv, k; \gamma) \tag{12}$$

$$= \left(H^\mathsf{T} W_k H\right)^{-1} H^\mathsf{T}\xi_k. \tag{13}$$

D. Composite Cost and Model Superposition

Multiple cost segments can be combined to achieve more complex filter characteristics. Such a combination of cost segments is called a *composite cost*, of which there are several variants [34].

To subsequently join P cost segments with individual decay factors $\gamma^{(p)}$ and interval borders a_p, b_p, we get the summed cost

$$\widetilde{J}(x, k) = \sum_{p=1}^{P} J_{a_p}^{b_p}(x, k; \gamma^{(p)}) \tag{14}$$

i.e.,

$$\widetilde{\kappa}_k = \sum_{p=1}^{P} \kappa_k^{(p)}, \tag{15}$$

$$\widetilde{\xi}_k = \sum_{p=1}^{P} \xi_k^{(p)}, \tag{16}$$

$$\widetilde{W}_k = \sum_{p=1}^{P} W_k^{(p)}. \tag{17}$$

While each segment in the composite cost has additionally assigned its individual output vector $c^{(p)}$ and decay factor $\gamma^{(p)}$, the transition matrix A and state vector x are common for all segments. This simplifies the subsequent computation, but is not a limitation of the method, since ALSSMs can be stacked. To superimpose Q models, we can apply

$$A = \operatorname{diag}\left(A^{(1)}, \dots, A^{(Q)}\right) \tag{18}$$

$$x = \begin{bmatrix}\left(x^{(1)}\right)^\mathsf{T} & \dots & \left(x^{(Q)}\right)^\mathsf{T}\end{bmatrix}^\mathsf{T} \tag{19}$$

$$c = \begin{bmatrix}c^{(1)} & \dots & c^{(Q)}\end{bmatrix} \tag{20}$$

E. Signal and Event Classification Using ALSSMs

Since a cost as in (4), or more generally (14), provides a measure of similarity between a model and the observed signal, we can use the costs to evaluate the performance of several models. We denote the ratio between two such cost remainders a *cost ratio*, which is closely related to the likelihood ratio of two alternative hypotheses in statistics. Since likelihoods are often in logarithmic scale, we analogously introduce the log-cost ratio

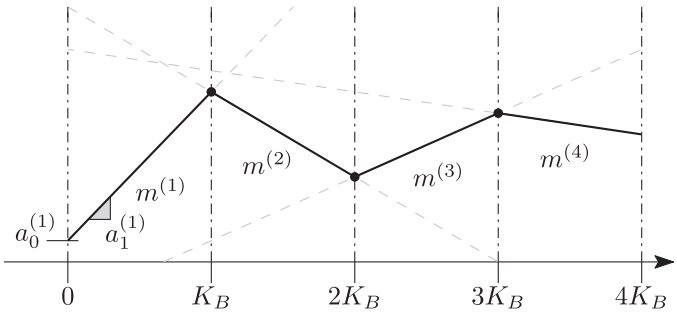

Fig. 2. Model of the amplifier drift artifact naturally occurring in intraoperative real-time Electrocochleography (rt-ECochG) when paralleled by real-time impedance measurements. The line segments are connected at the transition points of subsequent buffer cycles of the analog-to-digital converter.

(LCR)

$$\mathrm{LCR}_k = -\frac{1}{2}\log\frac{\min\limits_{x\in\mathcal{X}_1} J_a^b(x_1,k;\gamma_1)}{\min\limits_{x\in\mathcal{X}_2} J_a^b(x_2,k;\gamma_2)} \in \mathbb{R} \tag{21}$$

with $\mathcal{X}_1$ and $\mathcal{X}_2$ being distinct feature spaces [34].

F. Artifact Removal in ECochG Using ALSSMs

The currents injected by concurrent impedance measurements cause the analog amplifier of the ECochG measurement system to drift. As the polarity of these measurement currents alternate, the resulting drift artifact resembles a stationary triangular wave with the known period of a single buffer cycle. However, the exact slopes of the artifact depend on the electric properties of the surrounding tissue, which are unknown.

To compensate for the drift artifact, we design a piece-wise linear model (cf., Fig. 2) of Q continuous line segments. The model of line segment $q \in \{1,\dots,Q\}$ is

$$m_i^{(q)}(x) = a_0^{(q)} + a_1^{(q)} i. \tag{22}$$

The model is fitted to the raw measurement signal using a composite cost over the full epoch duration.

The ALSSM parametrization for a line model as in (22) is

$$A^{(q)} = \begin{bmatrix} 1 & 1 \\ 0 & 1 \end{bmatrix}, \quad c^{(q)} = \begin{bmatrix} 1 & 0 \end{bmatrix} \tag{23}$$

with state vector

$$x^{(q)} = \begin{bmatrix} a_0^{(q)} & a_1^{(q)} \end{bmatrix}^\mathsf{T}, \tag{24}$$

where a_0 reflects the line offset and a_1 the slope. A total of Q ALSSMs are then stacked according to (18)-(20) to obtain a composite cost (14). Each line model must connect to its successor, which is provided by the equality constraints

$$m_{qK_B}^{(q)} = m_{qK_B}^{(q+1)} \tag{25}$$

with K_B being the buffer size, i.e., the width of each line segment in number of samples. The cost segments match the buffer cycle width. The filter is thus evaluated only once, at $k = 0$. The constraints from (25) for $Q = 4$ are incorporated by applying (13) with

$$H = \begin{bmatrix} -K_B & K_B & K_B & 3K_B & 1 \\ 1 & 0 & 0 & 0 & 0 \\ 0 & -2K_B & K_B & 3K_B & 1 \\ 0 & 1 & 0 & 0 & 0 \\ 0 & 0 & -3K_B & 3K_B & 1 \\ 0 & 0 & 1 & 0 & 0 \\ 0 & 0 & 0 & 0 & 1 \\ 0 & 0 & 0 & 1 & 0 \end{bmatrix}. \tag{26}$$

The window functions are almost rectangular with a decay factor for reverse recursion $\gamma_{\leftarrow}^{(q)} = \frac{1000}{1000-1}$, $q \in \{2,\dots,Q\}$, except for the first window, where a slight decay was chosen with $\gamma_{\leftarrow}^{(1)} = \frac{0.5K_B}{0.5K_B-1}$ with $K_B = 60$ to emphasize the pre-stimulation baseline.

With this strategy, the signal is reconstructed by subtracting the artifact model trajectory from the raw epoch before the next processing step.

G. Noise Reduction in DIF Using ALSSMs

The morphology of a CM response is mainly determined by the acoustic stimulus [15]. This a priori knowledge enables to design a specific ALSSM filter that accurately reproduces the stimulation frequency f_0. To approximate the CM, we used a sinusoidal model of the form

$$m_i = \alpha \cdot \cos(\Omega_0 i + \phi) \tag{27}$$

with fixed frequency

$$\Omega_0 = 2\pi f_0 / f_s, \tag{28}$$

being normalized to the recording sampling rate f_s. The estimation parameters α and ϕ represent the amplitude and the phase of the sinusoidal. The ALSSM parametrization equivalent to (27) is

$$A = \begin{bmatrix} \cos\Omega & -\sin\Omega \\ \sin\Omega & \cos\Omega \end{bmatrix}, \quad c = \begin{bmatrix} 1 & 0 \end{bmatrix} \tag{29}$$

with state vector

$$x = \alpha \begin{bmatrix} \sin\phi & \cos\phi \end{bmatrix}^\mathsf{T}, \tag{30}$$

cf., Table I in [34]. For the composite cost window function, we chose a symmetric exponential decay with γ_l for $i = k+a \dots k$ and γ_r for $i = k+1 \dots k+b$. By adjusting the length and window shapes of the cost segment, filters of different frequency characteristics can be obtained. To form a bandpass filter, centered around f_0 as shown in Fig. 3, our model can simply be evaluated at $m_0(x)$ for every filter index k. By increasing the window width $L = b - a$, we observe the frequency specificity of the filter will also be increased. To preserve the frequency specificity of the filters for different stimulation frequencies, we adapt the window length accordingly.

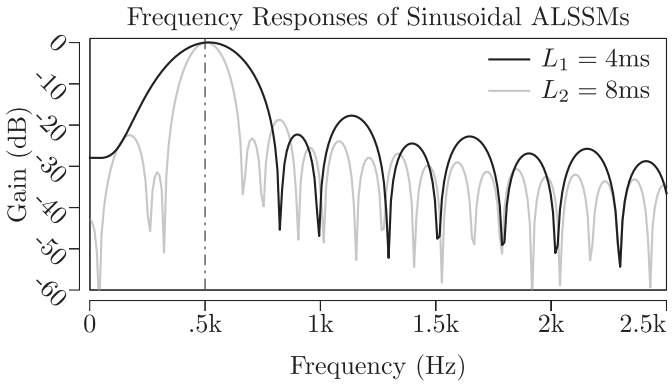

Fig. 3. Frequency responses of a sinusoidal Autonomous Linear State-Space Model (ALSSM) filter with ground frequency $f_0 = 500$ Hz and with two different window lengths L_1 and L_2 applying an exponentially decaying window. We note that wider windows (as with L_2) provide a higher frequency specificity of the filter. $L_1 = 4$ms, $L_2 = 8$ms.

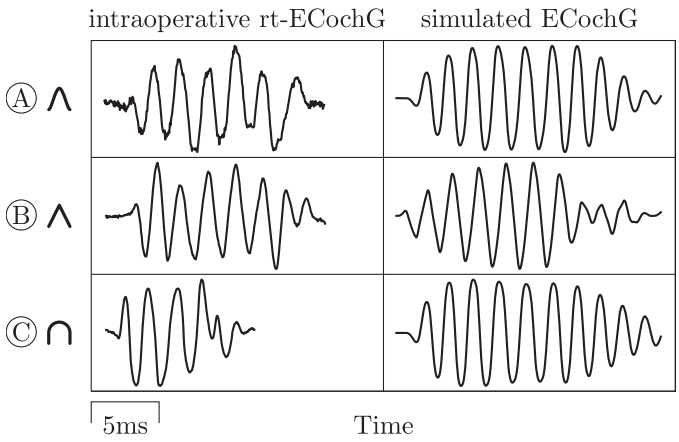

Fig. 4. Comparison of intraoperative real-time electrocochleography (rt-ECochG) responses to simulation data with normalized amplitudes. Shown are the difference signals (DIF) obtained by subtraction of responses from a condensation and rarefaction 500Hz acoustic pure tone stimulus. (a) DIF exhibiting sinusoidal peaks. (b) DIF exhibiting sharp peaks. (c) DIF exhibiting round peaks.

H. Morphological Analysis of the CM Using ALSSMs

The most commonly used feature to assess a CM response is the amplitude at the f_0-bin of the amplitude spectrum, obtained by fast Fourier transform (FFT) to the DIF epoch. In analogy, we extract the local amplitude and phase estimations $\hat{\alpha}_k$ and $\hat{\phi}_k$, respectively.

In a second step, we extract a confidence metric, how well our model (27) represents the observed data. For this, we compare the CM model (27) with a noise model by calculating

$$\mathrm{LCR}_k = -\frac{1}{2}\log \frac{\min\limits_{x\in\mathbb{R}^2}\left(J_a^0(x,k;\gamma_l) + J_1^b(x,k;\gamma_r)\right)}{J_a^0(\mathbf{0},k;\gamma_l) + J_1^b(\mathbf{0},k;\gamma_r)} \tag{31}$$

according to (21) [35]. Any $\mathrm{LCR} > 0$ indicates that the CM model explains the observation locally better than the noise model. To aggregate the amplitude information of a full epoch, we calculate an LCR-weighted average of the amplitudes. In doing so, plausible signal periods are emphasized. We parameterized the average with a window function (Hamming window) similar to the FFT to minimize windowing effects. The per-epoch average amplitude is therefore given by

$$\overline{\alpha} = \sum_{k=0}^{K} w_k \mathrm{LCR}_k \alpha_k \tag{32}$$

with w_i being the window function value. In analogy to (32), the per-epoch average

$$\overline{\mathrm{LCR}} = \sum_{k=0}^{K} w_k \mathrm{LCR}_k \tag{33}$$

is calculated to quantify an entire epoch.

I. Verification With Simulation Data

To test the suitability of the sinusoidal CM model, we performed a controlled sensitivity analysis of the amplitude estimation algorithm using simulated ECochG signals. Testing with simulation data allows to exclude external disturbances from the analysis and to examine the CM amplitude estimation separately from the artifact removal.

For signal synthesis, we used a verified open-source model of the auditory periphery by Zilany et al. [39], [40], [41], [42], [43], [44], [45]. This model allows to simulate IHC and OHC responses to a user-defined acoustic stimulus. We reproduced three typical ECochG waveforms (A, B and C) as seen during surgery by combining the simulated IHC and OHC cell potentials [45]. For each waveform, we varied the recruitment coefficients $C_{\mathrm{IHC}}, C_{\mathrm{OHC}} \in [0,1]$ of IHCs and OHCs as well as the intensity $I \in \mathbb{R}$ (in $\mathrm{dB_{SPL}}$, sound pressure level SPL) of the 11ms acoustic 500 Hz pure-tone stimulus in the simulation. The actual simulation parameters were A: $I = 60\mathrm{dB_{SPL}}, C_{\mathrm{IHC}} = C_{\mathrm{OHC}} = 1$, B: $I = 110\,\mathrm{dB_{SPL}}, C_{\mathrm{IHC}} = C_{\mathrm{OHC}} = 0.5$, C: $I = 60\,\mathrm{dB_{SPL}}, C_{\mathrm{IHC}} = 0, C_{\mathrm{OHC}} = 1$. Fig. 4 compares real intraoperative rt-ECochG recordings to the simulations. We added artificial pink noise to the signals to simulate different signal-to-noise ratios (SNRs).

For comparison, we also applied a commonly used conventional method on the same data set, which we reproduced to the best of our knowledge [20], [46]. In the conventional method, the discrete amplitude spectrum of the response is calculated using the FFT. The CM amplitude is then estimated using the f_0-bin of the spectrum's absolute values. To interpolate in frequency domain ($\Delta f \approx 25$Hz) and minimize leakage, the signal is zero-padded and multiplied with a Hamming window before the FFT. To estimate the noise level and its standard deviation, 3 preceding and 3 succeeding bins, starting 9 bins away from the f_0-bin are used [20]. With that, we also calculated the z-score of the f_0-bin.

We evaluated the performance of the algorithms using Monte Carlo simulations. The test includes estimations of the CM amplitude and an evaluation of response confidence metrics in the DIF signal for the three test waveforms (Fig. 4(a)–(c)). In the conventional method, the z-score was used as the confidence

metric. The performances of the different methods were evaluated with 10'000 samples per test waveform with SNRs in the range of $-10\,\mathrm{dB}$ to $+20\,\mathrm{dB}$.

J. Validation With Intraoperative Recordings

For illustration purposes, we applied the algorithms to a few exemplary patient data from an ongoing observational study and present the results graphically. More specifically, the real data presented throughout this paper come from five patients who averaged 59.2 years of age at implantation and had a pure tone average (PTA) of $76.7\,\mathrm{dB_{HL}}$ (hearing level HL).

We recorded rt-ECochG and rt-impedance data from CI patients during electrode insertion. The experimental study has been approved by the local institutional review board *Kantonale Ethikkommission Bern* (*Cantonal Ethics Committee of Bern*), Switzerland (BASEC ID 2019-01578) and was conducted in compliance with the Declaration of Helsinki. All participants or their legal guardian gave written informed consent before participating in the study.

Before the surgical incision, we placed a sterile insert foam eartip with a connected sound tube into the patient's external auditory canal [47], [48]. For stimulation, we connected the acoustic unit of a hybrid sound processor (*Nucleus 7*, Cochlear Ltd., Sydney, Australia) to the sound tube. Prior to insertion, we transcutaneously connected the sterile-packed transmitter coil of the sound processor to the implant. Insertion was then performed with pure tone stimulation and measurement of both rt-ECochG and impedance through the implant (*CI622*, Cochlear Ltd., Sydney, Australia) using the manufacturer's measurement software (*Cochlear Research Platform 2.0*, Cochlear Ltd., Sydney, Australia). The applied pure tone stimuli were 11 ms long and had an amplitude of either $100\,\mathrm{dB_{HL}}$ for 250 Hz or $108\mathrm{dB_{HL}}$ for 500 Hz. The epochs were recorded unfiltered over a window of 16 ms and a sampling rate of 20.5kHz. Impedance data were obtained using the default intraoperative setting of the *Cochlear Research Platform 2.0*, in which the monopolar impedances of all electrodes are measured simultaneously to rt-ECochG. The results of the measurements were not communicated to the surgeon until the insertion was complete. This was done to avoid influencing the insertion process.

We post-processed the collected data using our signal processing pipeline, which includes artifact removal, amplitude estimation, and LCR calculation. For comparison, we recorded the amplitude trace provided by the measurement software similar to the conventional method explained in Section II-I.

III. Results

A. Verification With Simulation Data

Fig. 5 compares the simulation results of the algorithms for determining the confidence metric of the CM responses for the three test waveforms (Fig. 4(a)–(c)). The top panel contains the results for the ALSSM method, while the bottom panel depicts the results of the conventional method. The curves show that the ALSSM method provides a more homogeneous result over

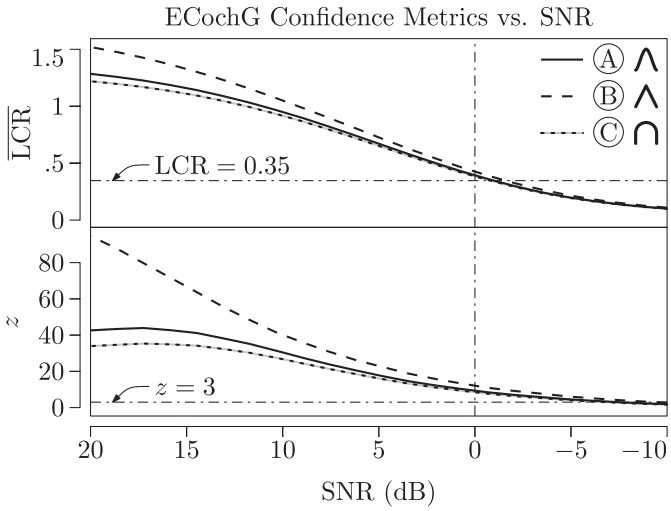

Fig. 5. Evaluation of confidence metrics for electrocochleography (ECochG) responses in simulation data at different signal-to-noise ratios (SNRs). The curves show mean values for $n = 10'000$ trials of three characteristic waveforms (Fig. 4(a)–(c)) with added random noise. Top panel: Logarithmic cost ratio (LCR) obtained by comparing a localized Autonomous Linear State-Space Model (ALSSM) of the cochlear microphonic (CM) versus a pure noise model. Bottom panel: z-score obtained by a FFT-based spectral estimation.

different CM shapes, especially in the range of distinct responses with $\mathrm{SNR} > 0\,\mathrm{dB}$.

As a first approach to establish a threshold for binary classification of the presence of physiological responses, we chose $\overline{\mathrm{LCR}} > 0.35$, where the cost of the CM model exceeds twice the cost of the noise model. As a result, signals for all test waveforms with $\mathrm{SNR} > -2\,\mathrm{dB}$ are being considered significant. Using the conventional method, on the other hand, even signals with $\mathrm{SNR} > -7.5\,\mathrm{dB}$ (waveforms A and C) and $\mathrm{SNR} > -10.3\,\mathrm{dB}$ (waveform B) are considered significant responses ($p < 0.01$).

Fig. 6 shows the relative absolute errors of the amplitude estimation comparing the ALSSM method and the conventional method at different SNRs. Each panel corresponds to the results of one of the three test waveforms (Fig. 4(a)–(c)).

The ALSSM estimated the CM amplitude more accurately in all simulations, and performed particularly well for waveforms (A) and (C). Both methods showed the largest error for waveform (B). The ALSSM method achieved a smaller error in this case as well. At SNRs $< -7.5\mathrm{dB}$, the estimation error of the ALSSM method is higher than the error of the conventional method. Since responses with such a low SNR are not considered significant by either method, the amplitude estimates in this range are invalid anyway.

B. Validation With Intraoperative Recordings

The top panel in Fig. 7 shows a raw DIF epoch from a rt-ECochG measurement distorted by the artifact as described in Section II-F together with the estimated artifact model trajectory. We reconstructed the signal as described in Section II-F (bottom panel). We applied the CM ALSSM (27) with $L = 2$ ms for noise reduction. By using the ALSSM as a bandpass filter, the transient

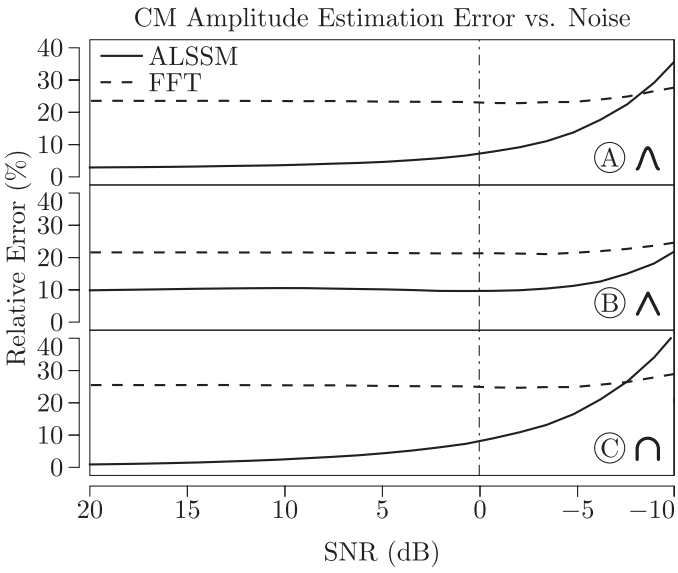

Fig. 6. Absolute errors of cochlear microphonic (CM) amplitude estimations in simulated electrocochleography (ECochG) data at different signal-to-noise ratios (SNRs). Each panel shows the averaged results for one of three characteristic waveforms (Fig. 4(a)–(c)) with added random noise from $n = 10'000$ trials. For comparison, the CM amplitudes were estimated by the new method using Autonomous Linear State-Space Models (ALSSM) and a conventional algorithm based on the fast Fourier transform (FFT).

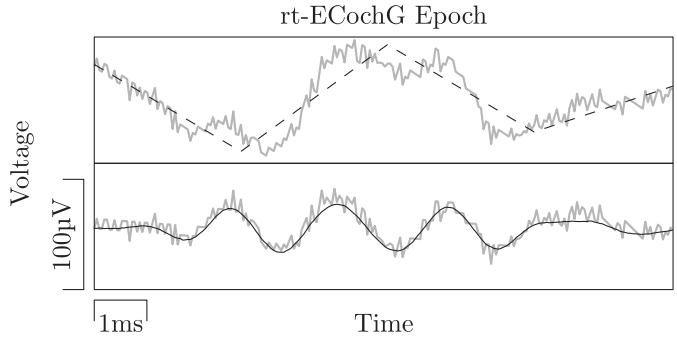

Fig. 7. Epoch from an intraoperative real-time electrocochleography (rt-ECochG) measurement, distorted by the amplifier drift artifact caused by concurrent real-time impedance measurements before and after application of the Autonomous Linear State-Space Model (ALSSM) filters. Top panel: Raw epoch before processing (*gray*) and artifact estimation (*black dased*). Bottom panel: Reconstructed signal before (*gray*) and after (*black*) noise reduction.

portions of the signal are reproduced. Note that the parameters of the localized model were also estimated at the same time.

Fig. 8 shows the pipeline result for a 250Hz pure-tone insertogram (i.e., rt-ECochG and rt-impedance measurements from the start of the electrode array insertion until full insertion), with three exemplary DIF epochs of different distortion and noise levels shown individually. The examples show that artifacts can be removed applying the artifact model. Further, the CM model fits well to the observed data within the window considered for the cost computations.

The result is an amplitude trace with artifacts removed, which at the same time retains its fast features. This becomes especially evident when comparing the ALSSM amplitude trace with the amplitude trace obtained using the conventional method. The intermediate rise in amplitude between 25 and 60 seconds as estimated by the conventional method coincides with the passage of the apical electrode through the round window at the start of the insertion (drop in apical impedance $|Z_{22}|$). This is not reproduced by the ALSSM method. Finally, the per-epoch average LCR provides an additional confidence metric.

Impedance traces of the apical (ICE 22) and basal (ICE 01) intracochlear electrodes are shown in the bottom panel to illustrate the entire insertogram. The impedance of the apical electrode elevates at 90 seconds, as expected due to the geometry of the cochlea, but then decreases towards the initial level [33], [49], [50], [51]. The impedance of the basal electrode drops sharply around 155 seconds after entering the fluid filled scala tympani. This event coincides with a spike in the CM amplitude estimate of the conventional method. However, this spike is not visible in the amplitude trace of the ALSSM method (Fig. 8, Epoch C).

IV. Discussion

We have implemented a signal processing pipeline for real-time morphological analysis of rt-ECochG signals. This signal processing pipeline includes artifact removal (IV-A), noise reduction (IV-B), and a local model for feature extraction (IV-C).

A. Artifact Removal

We demonstrated that artifacts caused by simultaneous rt-impedance measurements can be removed in rt-ECochG using our artifact ALSSM. The model-based approach allows the discontinuities of the artifact to be adequately represented. The estimation of the artifact becomes optimal when all other signal components are offset free over each single buffer cycle. However, the effects of this requirement are mitigated by constraining the individual models over the entire epoch. In addition, common modes of CON and RAR are eliminated in the DIF signal. In the future, the artifact parameters obtained with our approach potentially allows the derivation of intracochlear capacitive properties during the recording of an insertogram.

B. Noise Reduction

In the example from Fig. 7, we showed that the CM model is suitable for noise reduction in the DIF signal. The sinusoidal ALSSM behaves like a band-pass filter, which becomes less frequency specific when the window is shortened.

C. Feature Extraction

We used ALSSMs to locally fit a CM model to the observed data by estimating amplitude and phase. Simultaneously, we provided a confidence metric about the presence of a physiological response using LCR.

The simulations showed that the per-epoch average LCR yields similar results for all tested waveforms, and therefore is a

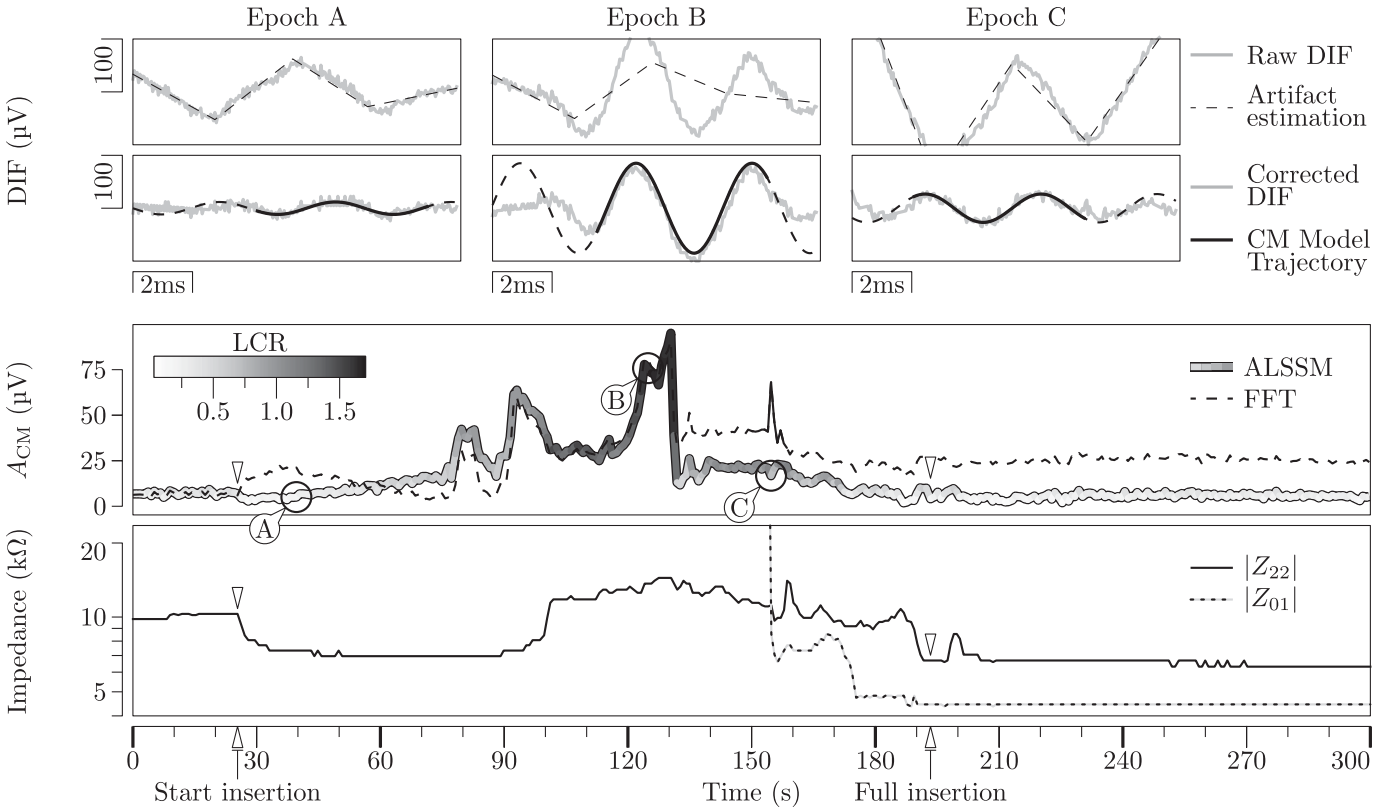

Fig. 8. Intraoperative real-time electrocochleography (rt-ECochG) with concurrent impedance measurements during cochlear implant (CI) electrode insertion. The rt-ECochG signals show the difference (DIF) of the responses obtained from condensation and rarefaction acoustic stimuli. The rt-ECochG was measured directly using the apical intracochlear electrode (ICE) of the CI. Top panels: Raw DIF epochs and artifact estimation using Autonomous Linear State-Space Models (ALSSM). The three epochs represent different groups of observed signals during surgery, namely (a) small response, heavily distorted by the impedance measurements, otherwise small SNR; (b) large response, distorted by the impedance measurements, low SNR; (c) medium response, heavily distorted by the impedance measurements, otherwise medium SNR. Second-top panels: Corrected DIF epochs after artifact removal and trajectories of locally fitted sinusoidal ALSSMs over the cost window width at the location of the maximum logarithmic cost ratio (LCR) representing the cochlear microphonic (CM). *Black, dashed:* Extrapolation of the CM model trajectory over the full epoch. Second-bottom panel: Estimated CM amplitude trace over the course of the CI electrode insertion obtained using the ALSSM method and the f_0-bin of the FFT. *Gray scale:* Per-epoch average LCR obtained using the ALSSM method. Bottom panel: Clinical impedance traces during CI electrode insertion, obtained from the apical (ICE-22) and basal (ICE-01) intracochlear electrodes.

more robust confidence metric for signal classification than the z-score from the conventional method. Thus, objective analysis for different rt-ECochG waveforms is facilitated with the novel ALSSM method. The steeper slope of the LCR curves relative to the dynamic range in the region of SNR $= 0$ dB implies a higher resolution of the confidence metric available for classifying the signals. Our first attempt to find a suitable threshold for binary classification of responses based on the LCR still needs refinement, since the classification with an LCR threshold of 0.35 showed to be rather conservative.

With the ALSSM method, the amplitude of simulated CM could be estimated more accurately than with the conventional method. The localized CM model provides a more detailed representation of the amplitudes in a single epoch. By weighting the individual amplitudes in an epoch using LCR, the per-epoch average amplitude can be estimated more robustly. The amplitude estimation for both methods could possibly be improved by considering the harmonics.

ECochG signals exhibit a rich morphology that includes features such as onset delay, phase, and envelope that could be used for trauma detection in the future. In a next step, it will be important to precisely determine these features by fitting a global CM model. In this context, the LCR and phase estimation of the CM ALSSM are indispensable [35], [36].

D. Study Limitations

The main limitation of the current study is the complexity of the CM model. To obtain a morphological description and feature set adequate for trauma detection, the full CM must be fitted with its transient components, in place of a local model. In addition, the artifact estimation could be improved by fitting a global CM model simultaneously with the artifact model, which is feasible with our approach, since ALSSMs can be stacked. Finally, ECochG response components other than the CM such as the auditory nerve neurophonic should be taken into account for trauma detection, so these must also be analysed.

The simulation data enable the evaluation of new algorithms for the analysis of intraoperative ECochG in a controlled sensitivity analysis. Still, the simulations do not correspond to

complete ECochG responses, but only reflect the cumulative cell potentials of the OHC and IHC clusters. To obtain more vivid ECochG simulations, a computer model of the cochlea is required [45].

The proposed signal processing pipeline has been illustrated by only few intraoperative examples. A prospective study in a larger clinical cohort is required to evaluate the classification performance of our approach.

V. Conclusion

We introduced a tool for the analysis of intraoperative real-time electrocochleography (rt-ECochG) based on Autonomous Linear State-Space Models (ALSSMs). The analysis includes artifact removal, noise reduction, and feature extraction together with a confidence metric (Logarithmic Cost Ratio, LCR) for the physiological response. Our signal processing pipeline enables the combination of rt-ECochG with simultaneously recorded impedance data for the purpose of improved automated trauma detection during cochlear implantation. We tested the feature extraction algorithms in simulated data and applied the full signal processing pipeline to a typical intraoperative measurement. The controlled sensitivity analysis with simulated data showed that our algorithms performed superior to conventional FFT-based methods. With our approach, it is feasible to perform a robust morphological analysis of the physiological response. Rt-ECochG waveforms can be described more efficiently with ALSSMs than with FFT. The LCR provides the means to automatically decide on the validity of a measured response. Since the presented algorithms are computationally efficient, they could be implemented on the implant itself for future applications other than intraoperative trauma detection, such as cochlear health monitoring while the patient wears the implant.

References

[1] R. H. Gifford et al., "Cochlear implantation with hearing preservation yields significant benefit for speech recognition in complex listening environments," *Ear Hear.*, vol. 34, no. 4, pp. 413–425, 2013.

[2] S. W. Sheffield et al., "Preserved acoustic hearing in cochlear implantation improves speech perception," *J. Amer. Acad. Audiol.*, vol. 26, no. 2, pp. 145–154, Feb. 2015.

[3] B. J. Gantz et al., "Preservation of hearing in cochlear implant surgery: Advantages of combined electrical and acoustical speech processing," *Laryngoscope*, vol. 115, no. 5, pp. 796–802, May 2005.

[4] B. J. Gantz et al., "Review: Clinical perspective on hearing preservation in cochlear implantation, the university of iowa experience," *Hear. Res.*, Mar. 2022, Art. no. 108487.

[5] L. Campbell et al., "Intraoperative real-time cochlear response telemetry predicts hearing preservation in cochlear implantation," *Otol. Neurotol.*, vol. 37, no. 4, pp. 332–338, Apr. 2016.

[6] D. Bakhos et al., "Electrophysiological exploration of hearing," *Eur. Ann. Otorhinolaryngol., Head Neck Dis.*, vol. 134, no. 5, pp. 325–331, 2017. [Online]. Available: https://www.sciencedirect.com/science/article/pii/S1879729617300509

[7] C. K. Giardina et al., "Response changes during insertion of a cochlear implant using extracochlear electrocochleography," *Ear Hear.*, vol. 39, no. 6, pp. 1146–1156, 2018.

[8] A. Dalbert et al., "Assessment of cochlear function during cochlear implantation by extra- and intracochlear electrocochleography," *Front. Neurosci.*, vol. 12, p. 18, 2018.

[9] A. Dalbert et al., "Simultaneous intra- and extracochlear electrocochleography during electrode insertion," *Ear Hear.*, vol. 42, no. 2, pp. 414–424, 2021.

[10] S. Weder et al., "Real time monitoring during cochlear implantation: Increasing the accuracy of predicting residual hearing outcomes," *Otol. Neurotol.*, vol. 42, pp. 1030–1036, Sep. 2021. [Online]. Available: https://journals.lww.com/otology-neurotology/Fulltext/2021/09000/Real_Time_Monitoring_During_Cochlear_Implantation_.16.aspx

[11] K. Schuerch et al., "Objectification of intracochlear electrocochleography using machine learning," *Front. Neurol.*, vol. 13, 2022, Art. no. 943816.

[12] A. Buechner et al., "Clinical experiences with intraoperative electrocochleography in cochlear implant recipients and its potential to reduce insertion trauma and improve postoperative hearing preservation," *PLoS One*, vol. 17, no. 4, pp. 1–16, 2022. [Online]. Available: https://doi.org/10.1371/journal.pone.0266077

[13] S. Wijewickrema et al., "Automatic analysis of cochlear response using electrocochleography signals during cochlear implant surgery," *PLoS One*, vol. 17, no. 7, 2022, Art. no. e0269187.

[14] C. Bester et al., "Electrocochleography triggered intervention successfully preserves residual hearing during cochlear implantation: Results of a randomised clinical trial," *Hear. Res.*, vol. 426, Dec. 2022, Art. no. 108353.

[15] P. Dallos et al., "Cochlear inner and outer hair cells: Functional differences," *Science*, vol. 177, no. 4046, pp. 356–358, Jul. 1972.

[16] P. Dallos and M. A. Cheatham, "Production of cochlear potentials by inner and outer hair cells," *J. Acoust. Soc. Amer.*, vol. 60, no. 2, pp. 510–512, Aug. 1976.

[17] S. O'Leary et al., "Monitoring cochlear health with intracochlear electrocochleography during cochlear implantation: Findings from an international clinical investigation," *Ear Hear.*, pp. 10–1097, 2022. [Online]. Available: https://journals.lww.com/ear-hearing/Fulltext/9900/Monitoring_Cochlear_Health_With_Intracochlear.73.aspx

[18] J. H. Barnes et al., "Electrocochleography in cochlear implantation: Development, applications, and future directions," *World J. Otorhinolaryngology - Head Neck Surg.*, vol. 7, no. 2, pp. 94–100, 2021. [Online]. Available: https://www.sciencedirect.com/science/article/pii/S2095881120300536

[19] C. K. Giardina et al., "Intracochlear electrocochleography: Response patterns during cochlear implantation and hearing preservation," *Ear Hear.*, vol. 40, no. 4, pp. 833–848, 2019.

[20] D. C. Fitzpatrick et al., "Round window electrocochleography just before cochlear implantation: Relationship to word recognition outcomes in adults," *Otol. Neurotol.*, vol. 35, no. 1, pp. 64–71, Jan. 2014.

[21] T. E. Fontenot et al., "A model-based approach for separating the cochlear microphonic from the auditory nerve neurophonic in the ongoing response using electrocochleography," *Front. Neurosci.*, vol. 11, 2017, Art. no. 592.

[22] B. Krüger et al., "Amplitude growth of intracochlear electrocochleography in cochlear implant users with residual hearing," *J. Acoust. Soc. Amer.*, vol. 147, no. 2, 2020, Art. no. 1147.

[23] K. Koka et al., "Electrocochleography in cochlear implant recipients with residual hearing: Comparison with audiometric thresholds," *Ear Hear.*, vol. 38, no. 3, pp. e161–e167, 2017.

[24] M. S. Harris et al., "Patterns seen during electrode insertion using intracochlear electrocochleography obtained directly through a cochlear implant," *Otol. Neurotol.*, vol. 38, no. 10, pp. 1415–1420, 2017.

[25] L. Sijgers et al., "Simultaneous intra- and extracochlear electrocochleography during cochlear implantation to enhance response interpretation," *Trends Hear.*, vol. 25, 2021, Art. no. 2331216521990594.

[26] S. Weder et al., "Toward a better understanding of electrocochleography," *Ear Hear.*, vol. 41, pp. 1560–1567, Nov./Dec. 2020. [Online]. Available: https://journals.lww.com/ear-hearing/Fulltext/2020/11000/Toward_a_Better_Understanding_of.13.aspx

[27] Y. Dong et al., "Detection of translocation of cochlear implant electrode arrays by intracochlear impedance measurements," *Ear Hear.*, vol. 42, no. 5, pp. 1397–1404, 2021.

[28] W. Wimmer et al., "Cochlear implant electrode impedance as potential biomarker for residual hearing," *Front. Neurol.*, vol. 13, 2022, Art. no. 886171.

[29] C. Bester et al., "Four-point impedance as a biomarker for bleeding during cochlear implantation," *Sci. Rep.*, vol. 10, no. 1, 2020, Art. no. 2777.

[30] C. Shaul et al., "Electrical impedance as a biomarker for inner ear pathology," *Otol. Neurotol.*, vol. 40, pp. 518–526, Jun. 2019. [Online]. Available: https://journals.lww.com/otology-neurotology/Fulltext/2019/06000/Electrical_Impedance_as_a_Biomarker_for_Inner_Ear.16.aspx

[31] J. Choi et al., "Electrode impedance fluctuations as a biomarker for inner ear pathology after cochlear implantation," *Otol. Neurotol.*, vol. 38, no. 10, pp. 1433–1439, 2017.
[32] S. Schraivogel et al., "Postoperative impedance-based estimation of cochlear implant electrode insertion depth," *Ear Hear.*, 2023.
[33] F. A. Di Lella et al., "Measuring the electrical status of the bionic ear. rethinking the impedance in cochlear implants," *Front. Bioeng. Biotechnol.*, vol. 8, 2020, Art. no. 568690. [Online]. Available: https://www.frontiersin.org/article/10.3389/fbioe.2020.568690
[34] R. A. Wildhaber et al., "Windowed state-space filters for signal detection and separation," *IEEE Trans. Signal Process.*, vol. 66, no. 14, pp. 3768–3783, Jul. 2018.
[35] E. Ren, G. C. Ornelas, and H.-A. Loeliger, "Real-time interaural time delay estimation via onset detection," in *Proc. IEEE Int. Conf. Acoust., Speech Signal Process.*, 2021, pp. 4555–4559.
[36] F. Waldmann et al., "Onset detection of pulse-shaped bioelectrical signals using linear state space models," *Curr. Directions Biomed. Eng.*, vol. 8, no. 2, pp. 101–104, 2022. [Online]. Available: https://doi.org/10.1515/cdbme-2022-1027
[37] R. A. Wildhaber et al., "LMLIB – An open source model-based signal processing library," 2022. [Online]. Available: https://lmlib.ch/
[38] N. Zalmai, "A state space world for detecting and estimating events and learning sparse signal decompositions," Ph.D. dissertation, Doctor of Sci., ETH Zurich, Zürich, Switzerland, 2017. [Online]. Available: https://doi.org/10.3929/ethz-b-000176652
[39] M. S. Zilany and I. C. Bruce, "Modeling auditory-nerve responses for high sound pressure levels in the normal and impaired auditory periphery," *J. Acoust. Soc. Amer.*, vol. 120, no. 3, pp. 1446–1466, Sep. 2006.
[40] M. S. Zilany et al., "Updated parameters and expanded simulation options for a model of the auditory periphery," *J. Acoust. Soc. Amer.*, vol. 135, no. 1, pp. 283–286, Jan. 2014.
[41] L. H. Carney, "A model for the responses of low-frequency auditory-nerve fibers in cat," *J. Acoust. Soc. Amer.*, vol. 93, no. 1, pp. 401–417, Jan. 1993.
[42] X. Zhang et al., "A phenomenological model for the responses of auditory-nerve fibers: I. nonlinear tuning with compression and suppression," *J. Acoust. Soc. Amer.*, vol. 109, no. 2, pp. 648–670, Feb. 2001.
[43] I. C. Bruce et al., "An auditory-periphery model of the effects of acoustic trauma on auditory nerve responses," *J. Acoust. Soc. Amer.*, vol. 113, no. 1, pp. 369–388, Jan. 2003.
[44] I. C. Bruce et al., "A phenomenological model of the synapse between the inner hair cell and auditory nerve: Implications of limited neurotransmitter release sites," *Hear. Res.*, vol. 360, pp. 40–54, 2018.
[45] M. J. van Gendt et al., "Simulating intracochlear electrocochleography with a combined model of acoustic hearing and electric current spread in the cochlea," *J. Acoust. Soc. Amer.*, vol. 147, no. 3, 2020, Art. no. 2049.
[46] M. Forgues et al., "Distinguishing hair cell from neural potentials recorded at the round window," *J Neurophysiol*, vol. 111, no. 3, pp. 580–593, Feb. 2014.
[47] K. Schuerch et al., "Increasing the reliability of real-time electrocochleography during cochlear implantation: A standardized guideline," *Eur. Arch. Otorhinolaryngol.*, vol. 279, no. 10, pp. 4655–4665, Oct. 2022.
[48] K. Schuerch et al., "Performing intracochlear electrocochleography during cochlear implantation," *J. Vis. Exp.*, vol. 181, 2022, Art. no. e63153.
[49] P. Aebischer et al., "Intraoperative impedance-based estimation of cochlear implant electrode array insertion depth," *IEEE Trans. Biomed. Eng.*, vol. 68, no. 2, pp. 545–555, Feb. 2021.
[50] F. A. Di Lella et al., "In vivo real-time remote cochlear implant capacitive impedance measurements: A glimpse into the implanted inner ear," *Otol. Neurotol.*, vol. 40, no. 5S, pp. S18–S22, 2019.
[51] C. K. Giardina et al., "Impedance measures during in vitro cochlear implantation predict array positioning," *IEEE Trans. Biomed. Eng.*, vol. 65, no. 2, pp. 327–335, Feb. 2018.